


Article

Biochar-Supported Titanium Oxide for the Photocatalytic Treatment of Orange II Sodium Salt

Laury Kanku , Kassim Olasunkanmi Badmus *  and Fracois Wewers

Chemistry Department, Cape Peninsula University of Technology, P.O. Box 1906, Cape Town 7535, South Africa; laurhymusungay52@gmail.com (L.K.); wewersf@cput.ac.za (F.W.)

* Correspondence: racetech23.kb@gmail.com; Tel.: +23-49060397156

Abstract: Recent improvements in advanced technology for toxic chemical remediation have involved the application of titanium oxide nanoparticles as a photocatalyst. However, the large energy bandgap associated with titanium oxide nanoparticles (3.0–3.20 eV) is a limitation for their application as a photocatalyst within the solar spectrum. Various structural modification methods have led to significant reductions in the energy bandgap but not without their disadvantages, such as electron recombination. In the current investigation, biochar was made from the leaves of an invasive plant (*Acacia saligna*) and subsequently applied as a support in the synthesis of titanium oxide nanoparticles. The characterization of biochar-supported titanium oxide nanoparticles was performed using scanning electron microscopy, Fourier transformer infrared, X-ray diffraction, and Brunauer–Emmett–Teller analyses. The results showed that the titanium oxide was successfully immobilized on the biochar's external surface. The synthesized biochar-supported titanium oxide nanoparticles exhibited the phenomenon of small hysteresis, which represents the typical type IV isotherm attributed to mesoporous materials with low porosity. Meanwhile, X-ray diffraction analysis revealed the presence of a mixture of rutile and anatase crystalline phase titanium oxide. The synthesis of biochar-supported titanium oxide nanoparticles was highly efficient in the degradation of Orange II Sodium dye under solar irradiation. Moreover, 83.5% degradation was achieved when the biochar-supported titanium oxide nanoparticles were used as photocatalysts in comparison with the reference titanium oxide, which only achieved 20% degradation.



Citation: Kanku, L.; Badmus, K.O.; Wewers, F. Biochar-Supported Titanium Oxide for the Photocatalytic Treatment of Orange II Sodium Salt. *Appl. Nano* **2024**, *5*, 190–204. <https://doi.org/10.3390/applnano5030013>

Academic Editors: Sara Cerra and Ilaria Fratoddi

Received: 30 June 2024

Revised: 2 August 2024

Accepted: 19 August 2024

Published: 19 September 2024



Copyright: © 2024 by the authors. Licensee MDPI, Basel, Switzerland. This article is an open access article distributed under the terms and conditions of the Creative Commons Attribution (CC BY) license (<https://creativecommons.org/licenses/by/4.0/>).

Keywords: photocatalyst; nanoparticle; titanium (IV) oxide; biochar; degradation; synthesis

1. Introduction

Heterogeneous photocatalysts are extensively used for wastewater treatment because of their higher effectiveness in the removal of recalcitrant pollutants and harmful bacteria during UV solar irradiation [1]. The process is based on the photoactivation of semiconductor nanoparticles (TiO_2 , SiO_2 , Al_2O_3 , and ZnS) through visible light irradiation. Photocatalytic oxidation leads to the generation of reactive oxidizing species (commonly the OH radical), which can cause the degradation of organic pollutants and the denaturation of microbes [2]. The photoactivation of nanomaterials can be understood as the transition of an electron (e^-) from the valence band (VB) to the conduction band (CB) at an ambient temperature due to the absorption of photons having equal or higher energy than the bandgap energy [3]. This absorption generates oxidizing sites known as holes (h^+) in the valence band, which may react directly with the pollutants. This process can lead to the total degradation of toxic pollutants to harmless species such as carbon dioxide and water [4]. The mechanism of photocatalytic activation in TiO_2 has been demonstrated previously [5].

Titanium oxide is an ideal semiconductor nanoparticle for use in photocatalytic processes due to its thermochemical stability, cost-effectiveness, availability, high reactivity under light irradiation, and low toxicity [6]. The high chemical stability of titanium oxide is

one of its major advantages over other common heterogeneous photocatalysts [7]. However, it shows photophysical limitations due to its large energy bandgap (3.0–3.20 eV), which limits its activity to only the UV range [8]. Reductions in the energy bandgap of titanium oxide will facilitate its application as a photocatalyst and enhance the photophysical utilization of a larger percentage of natural solar light (the electromagnetic spectrum). This can be achieved through structural modifications of titanium oxide [9].

2. Titanium Oxide Modifications for Enhanced Solar Activities

The principal objective of titanium oxide modifications is related to the reduction in its energy bandgap. Thus, it requires moving its optical response from the UV region to the visible region and reducing the electron–hole pair recombination. Modification techniques for the enhancement of the photophysical performance of titanium oxide include doping with metals and non-metals, dye sensitization, deposition with noble metals, and a coupled semiconductor. Previous studies have shown that doping has a positive effect on titanium oxide because it introduces elements such as metals and non-metals to the titanium structure, which leads to an increase in its photo-activity by changing its functional properties [10,11]. The impact of doping on photocatalysts is regulated by certain factors such as the nature of the dopants, the synthesis process, and the physicochemical properties of the photocatalyst [2,12].

2.1. Metal Ion Doping

The modification of titanium oxide with metal ions (transition metals) such as Pt, Au, Ag, Cu, V, Ni, and Sn has been discovered to shift its photo-response and photocatalytic activity into the visible light region (Shuying et al., 2015). Metal ion doping can lead to the duplication of the conduction band (CB) in titanium by the *d*-orbital of the transition metal, leading to a decrease in the energy bandgap [13]. The newly created energy levels between the valence band (VB) and conduction band (CB) ensure the transfer of electrons into the visible light region of the electromagnetic spectrum [14]. The metal ion may cross the optimum limit at a very low concentration and act as a recombination center for charge carriers by causing photoactivity. The existence of an acceptable quantity of metal ion doping (optimum limit) guarantees that the metal particles simply appear as electron traps, thus helping the electron–hole split [15]. Transition metal ions can also play the role of recombination sites for photo-induced charge carriers, therefore decreasing the quantum effectiveness [13,16]. Furthermore, metal ion doping may enhance the rate of electron/hole recombination and generate a thermal imbalance. It is then essential to prevent this by considering the effective quantity of the metal ion during the synthesis of the doped titanium oxide nanoparticles. Doping with more than one metal oxide such as SiO₂, ZrO₂, WO₃, Fe₂O₃, SnO₂, Ln₂O₃, and RuO₂ may invariably lead to an enhancement in the photocatalytic effectiveness and a diminishment in the energy bandgap by causing structure modifications in titanium oxide [17]. Moreover, electron–hole pair recombination may also arise as a consequence of the thermodynamic imbalance in some metal oxides (RuO₂/TiO₂) [13].

2.2. Non-Metal Doping

The doping of titanium oxide with non-metals (such as C, F, B, S, N, and Br) has been widely investigated due to the relatively high photo-stability of titanium-doped non-metals [18]. The main goal of non-metal-doped titanium oxide is to ensure a decrease in the recombination of electron–hole pairs [19]. Usually, it involves oxygen atom substitution by the non-metal in the titanium lattice for a targeted decrease in the bandgap and electron recombination prevention [20]. Notably, non-metal doping at the atomic level can maintain the intrinsic surface properties of titanium oxide. The dopant non-metal mostly acts as an isolated particle instead of clusters throughout the surface [18]. Moreover, the exceptional distribution of dopant states is usually found to be almost more than the VB maximum, making the photo-generated holes on these states oxidative enough for further photoreactions.

2.3. Titanium Oxide-Supported Carbon Composites in Photocatalysis

Extensive studies have been performed on the photocatalytic activity of titanium oxide-supported carbon for the degradation of organic pollutants [21–23]. Singh et al. (2016) studied the degradation of Direct Blue 199 dye using activated carbon-based TiO₂ nanocomposites under 196 W mini lamps [24]. They also studied the reaction kinetic model of the photocatalytic, sonocatalytic, and sono-photocatalytic processes. Their results showed that the sono-photocatalytic process showed maximum degradation. However, the photocatalytic reactor was more efficient because it consumed less energy. The authors also demonstrated that the degradation reactions of Direct-blue 199 followed the Langmuir–Hinshelwood model. Rashed et al. (2017) studied the adsorption and photocatalysis of methyl orange and cadmium (Cd) removal from wastewater using TiO₂/sewage sludge-based activated carbon nanocomposites under (15 W) UV irradiation lamps [4]. They also investigated the factors influencing photocatalysis such as the amount of TiO₂, initial pollutant concentrations, solution pH, nanocomposite dosage, and UV irradiation time. Their results revealed that these factors have a direct influence on the photocatalyst's efficiency. Nguyen et al. (2020) studied the kinetics of adsorption and photocatalysis in the removal of phenol, naphthol blue black, and reactive black 5, under UV lamps [25]. Their kinetic analysis revealed that the adsorption-assisted photocatalysis performance depended on the similarity of the initial rates of adsorption and degradation determined by the properties of the photocatalyst and that of the dye. Mondol et al. (2021) synthesized activated carbon/TiO₂ nano-hybrids by a hydrothermal technique [26]. They studied the photocatalytic activity by photodegradation of Reactive Red-35 dye using solar irradiation in open air. Their report showed that the photodegradation was mainly controlled by radicals such as •OH and •O₂[−]. The photocatalytic performance was significant due to the synergistic effect of adsorption and the photodegradation activity of the nano-hybrids. Despite the research effort in the synthesis of activated carbon/TiO₂ nanocomposites, there are challenges in the preparation process timeline, calcination temperatures, and chemical reagents. Therefore, there is a need to apply an energy-efficient and simple preparation method which will ensure fast production process, cost-effectiveness, and low energy use. Hydrothermal synthesis is well known for its tremendous advantages. It has potential for reduced in-process reduction, continuous catalyst activation, and industrial-scale production. It is also important to consider the sources and economic advantages when choosing the carbon material for the production of biochar. Various sources of carbon have been investigated for their benefits in the biochar production. However, most trial cases have supported the use of end-of-life biomass (ELB) such as sewage sludge, animal manure, and agricultural residues as a feedstock [27]. The use of invasive plants can play an important role in reduction of carbon sequestration and unprofitable application of weedicide to control them. The fast production and strong environmental adaptability of invasive plants make them harmful to the environment. The valorization of these plants, therefore, aids their control and management. In addition, previous studies have focused on UV irradiation, which requires difficult and expensive maintenance [28,29]. The achievement of a low cost and sustainability in the treatment of industrial wastewater can only be attained through the exploitation of abundant solar energy and application of an efficient photocatalyst.

3. Port Jackson Willow (*Acacia saligna*)

The Port Jackson willow (PJ) is a flexible tree that grows rapidly in semi-desert regions (including South Africa), and it is used as a windscreen and as an ornamental tree. It has become an invasive species outside of its natural range, threatening biological diversity, and is categorized as an Invasive Alien Plant (IAP) [27]. IAPs have a negative impact on the ecosystem by consuming more water than local plants, exhausting valuable water resources, and also providing material for wildfires, making them exceptionally hot, which destroys the soil structure and sterilizes the soil for up to three years. This results in negative ecological, social, and economic impacts.

3.1. Chemical Reagents and Materials

The chemicals used in the current investigations included hydrochloric acid ($\geq 37\%$), nitric acid (65%), ethanol ($\geq 99\%$), titanium (III) trichloride solution ($\geq 12\%$), and Orange II Sodium salt ($\geq 85\%$). They were purchased from Sigma Aldrich. Port Jackson willow leaves were obtained from the Cape Flats forest and identified at the Department of Botany, University of Cape Town.

3.2. Preparation of Biochar

Biochar was prepared by pyrolysis of the Port Jackson willow leaves. The collected leaves were washed several times with deionized water to remove dust and other impurities, dried, and ground into powdered form. An amount of the dried powdered leaves equal to 10.0 g was put in a Teflon crucible to prevent the leaching of unwanted elements during the carbonization. Thereafter, the dried powdered leaves were subjected to carbonization in the oven at 250 °C for 2 h (with limited air supply) to obtain a biochar.

4. Synthesis of the Titanium Oxide Nanoparticles

Titanium dioxide (TiO₂) was prepared using TiCl₃ (Fluka 15% solution) as a precursor. Firstly, TiCl₃ (7 mL) was subjected to acid hydrolysis by the addition of 1.5 mL of HCl (10%), and the mixture was diluted in distilled water (9 mL) and stirred for 15 min to ensure maximum homogenization. The reaction temperature was increased by boiling the obtained solution in a water bath at 80 °C for 10 min before the oxidation by slowly adding 6 mL of concentrated HNO₃. The heating in the water bath was continued for 10 h. The resulting high-purity titanium oxide nanoparticles were washed with deionized water and recovered through centrifugation.

Synthesis of Biochar-Supported TiO₂ Nanocomposite

The biochar-supported titanium oxide nanoparticles were obtained by mixing the 200 mg of synthesized titanium oxide nanoparticles with 50 mg of biochar and dissolving the mixture in ethanol (10 mL). The mixture was then subjected to sonication for about 1 h at room temperature to ensure homogeneity and the effective incorporation of titanium on the biochar support. The solution was dried in the oven for 2 h at 80 °C. The resulting samples were subjected to calcination under a nitrogen (N₂) stream at 500 °C for 3 h. The obtained powder was washed with 50 mL of ethanol (30%) and dried in a desiccator. The procedure was repeated at varied ratios of biochar to titanium oxide (2:1, 2:2, 2:3, and 2:4).

5. Energy Bandgap Determination

The energy bandgap of a semiconductor is the needed energy for the excitement of its electron to move from the valence band to the conduction band. This is important in predicting the photophysical and photochemical properties of semiconductors. The method is based on the assumption that the energy bandgap is dependent on the absorption coefficient of a photocatalyst (Equation (1))

$$(\alpha hv)^2 = K(hv - E_g) \quad (1)$$

where h is the Planck constant, v is the photon's frequency, E_g is the energy bandgap, K is a constant, and hv is the energy of the incident wave.

The calculated energy bandgap for the prepared biochar-supported titanium oxide nanoparticles at varied amounts of biochar is presented in Table 1.

It was discovered that biochar/TiO₂ at a 2:3 ratio gave the smallest energy bandgap (1.96 eV). This biochar/TiO₂ ratio was considered as the optimum for the synthesis of a biochar-supported TiO₂ photocatalyst, and it was used for further characterizations and application.

Table 1. The energy bandgap of the synthesized titanium oxide as calculated from Tauc plots.

Weight of TiO ₂ (mg)	Weight of Biochar (mg)	Ratio	Energy Bandgap (eV)
200	50	4:1	2.52
200	100	2:1	2.50
200	200	1:1	2.49
200	300	2:3	1.96
200	400	1:2	2.12
200	500	2:5	2.33

5.1. Characterization of Biochar Obtained from PJW Leaves

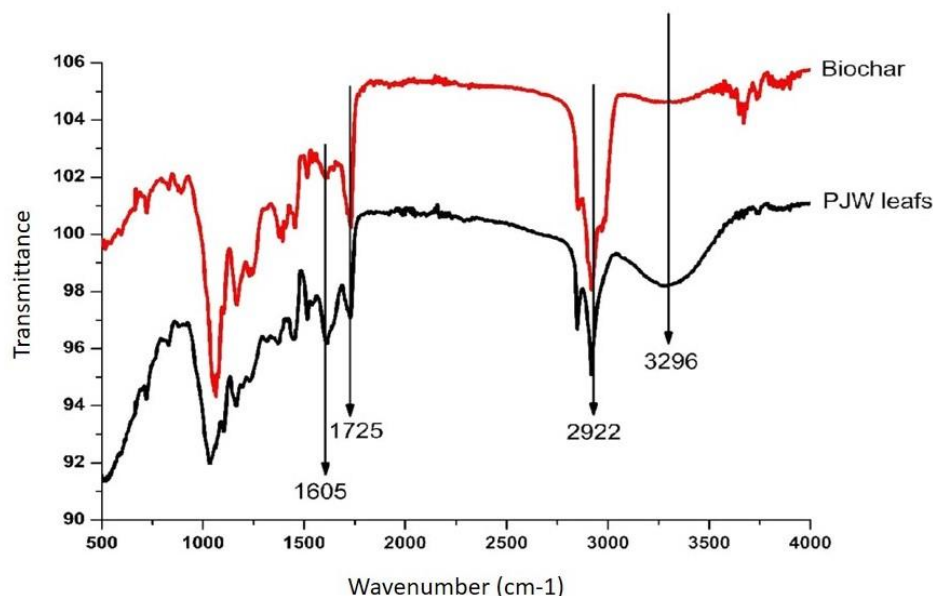
The obtained yield of Biochar after the carbonization of the PJW leaves is presented in Table 2. An increased pyrolysis period (from 1 to 3 h) led to a reduction in biochar yield from 70.58 to 68.90%. The decreased yield of biochar at this point may be attributed to the combustion of the retained organic materials and the elimination of retained volatile organic compounds.

Table 2. Yield and chemical compositions of the biochar from PJW leaves [PJW leaf weight = 10.0 g; temperature = 250 °C].

Pyrolysis Time (h)	Yield (%)	Carbon (%)	Oxygen (%)	Other Elements (%)
1	68.90	78.62	19.05	2.33
2	70.90	75.11	22.26	2.63
3	70.58	77.57	19.30	3.14

5.2. Functional Group Identification

The Fourier transform infrared (FT-IR) spectra of the PJW leaves and the prepared biochar are presented in Figure 1. The band at 3296 cm⁻¹ attributed to the -OH stretching vibration due to the surface-adsorbed moisture or hydroxyl group was observed in the FT-IR spectra of the PJW sample, but this peak was less pronounced in the resulting biochar. The -CH₂- symmetric stretch peaks of an alkyl at 2992 cm⁻¹ were also observed on the FT-IR spectra of both PJW leaves and the prepared biochar. Meanwhile, the C=O stretching vibration at 1725 cm⁻¹ and the C=C stretching variation aromatic ring were present in both the PJW leaves and the prepared biochar.

**Figure 1.** FTIR spectra of PJW leaf and biochar.

It was noted that all the functional groups prominent in the PJW leaves were retained in biochar after the carbonization. However, the FT-IR spectra in the fingerprint region of both PJW leaves and the prepared biochar were not similar. There was an improvement in the acidic functional groups on the produced biochar surface in comparison with the PJW. This is an indication that the PJW leaves have been converted to an entirely new product by their carbonization [30].

5.3. Surface Morphology of the Prepared Biochar

The produced biochar from the carbonization of PJW has significantly oxygenated functional groups on its surface, as presented by scanning electron microscope (SEM) analysis (Figure 2). There was a clear reduction in the surface porosity of the produced biochar. The superiority of the surface oxidized biochar in terms of its hydrophilicity was reported by Singh et al. (2016) [31]. The high hydrophilicity and wettability of the biochar surface are very important for an enhanced binding with metals.

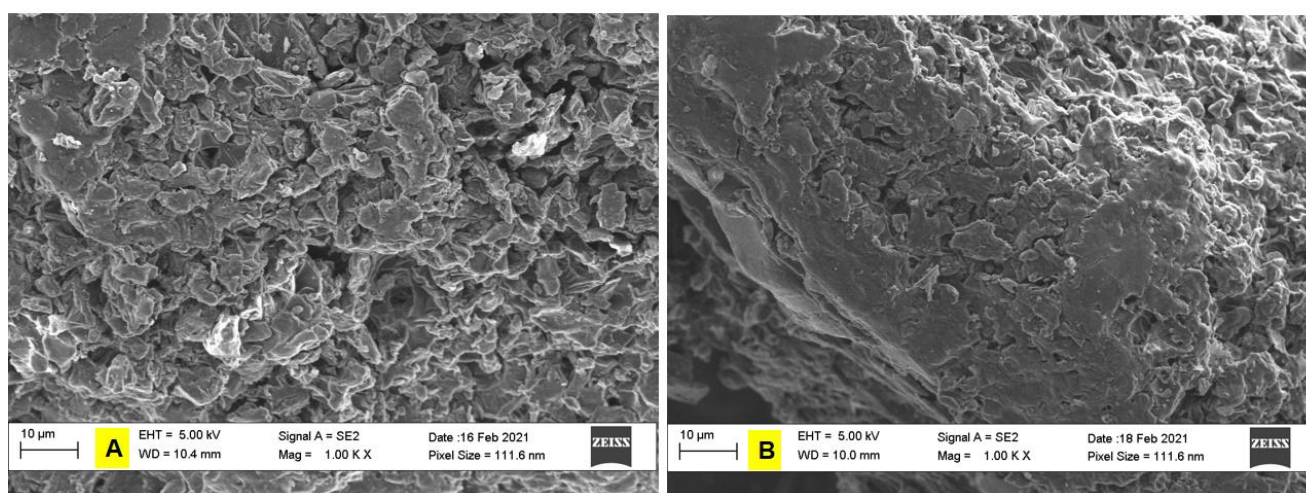


Figure 2. SEM images of PJW leaves (A) and the produced biochar (B).

5.4. Energy Bandgap of Biochar-Supported Titanium Oxide

The energy bandgaps of the synthesized titanium oxide and the biochar-supported titanium oxide nanoparticles were measured using Tauc plots. It was observed that the energy bandgap of the synthesized titanium oxide nanoparticles and that of the biochar-supported titanium oxide nanoparticles were 2.81 eV and 1.96 eV, respectively. The significant reduction in the energy bandgap of biochar-supported titanium oxide nanoparticles was a result of an alteration in the structure of Ti-O-C bonds. The carbon $2p$ can interact with oxygen $2p$ atomic orbitals in an inert reaction environment (nitrogen) to produce sub-band levels between the valence band (VB) and conduction band (CB) [32]. The observed increases in the edge of the valence band consequently caused a reduction in the energy bandgap [18]. In the current investigation, the application of PJW biochar as a support for titanium oxide led to a significant modification in the morphological structure and reduction in the energy bandgap. The biochar-supported titanium oxide nanoparticles showed greater promise as a solar-active photocatalyst.

5.5. SEM-EDS of the Synthesized Titanium Oxide Nanoparticles

The scanning electron microscopy and energy-dispersive X-ray spectroscopy (SEM-EDS) of the titanium oxide showed oxygen (41.10%) and titanium (43.45%) were present in a near similar ratio, indicating the formation of titanium oxide nanoparticles in their pure form (Table 3). Meanwhile, the SEM-EDS result for the biochar-supported titanium oxide nanoparticles showed oxygen (39.71%), titanium (24.29%), and carbon (34.49%) as the main elements in the nanocomposite. The increase in the % composition of carbon is a direct

effect and an indication of the successful incorporation of titanium within the mesoporous biochar. Likewise, an observed increased oxygen–titanium ratio was due to the formation of new oxygen bonds. The resultant oxygen vacancy is responsible for a lower energy gap and consequently a reduction in electron recombination associated with the titanium oxide nanoparticles.

Table 3. SEM-EDS showing the chemical composition of the synthesized titanium oxide and biochar-supported titanium oxide nanoparticles.

Elements	TiO ₂ (Wt %)	Biochar-Supported TiO ₂ (Wt %)
Titanium	43.45	24.29
Oxygen	41.40	39.71
Carbon	15.14	34.59
K	-	0.61

5.6. Brunauer–Emmett–Teller (BET) Surface Area Analysis

The N₂ adsorption–desorption isotherms of the synthesized titanium oxide and biochar-supported titanium oxide nanoparticles are presented in Figure 3. The adsorption–desorption isotherms exhibit the characteristics of mesoporous solids resulting in type IV adsorption isotherms undergoing capillary condensation and hysteresis during desorption [33]. Different parameters were obtained for the Brunauer–Emmett–Teller (BET) method surface area and Barrett–Joyner–Helanda (BJH) method pore size distribution. The BET surface area and adsorption average pore diameter of synthesized titanium oxide were 11.11 m²/g and 9.793 Å, respectively. And for the biochar-supported titanium oxide nanoparticles, the BET surface area and adsorption average pore diameter were 84.45 m²/g and 10.12 Å, respectively.

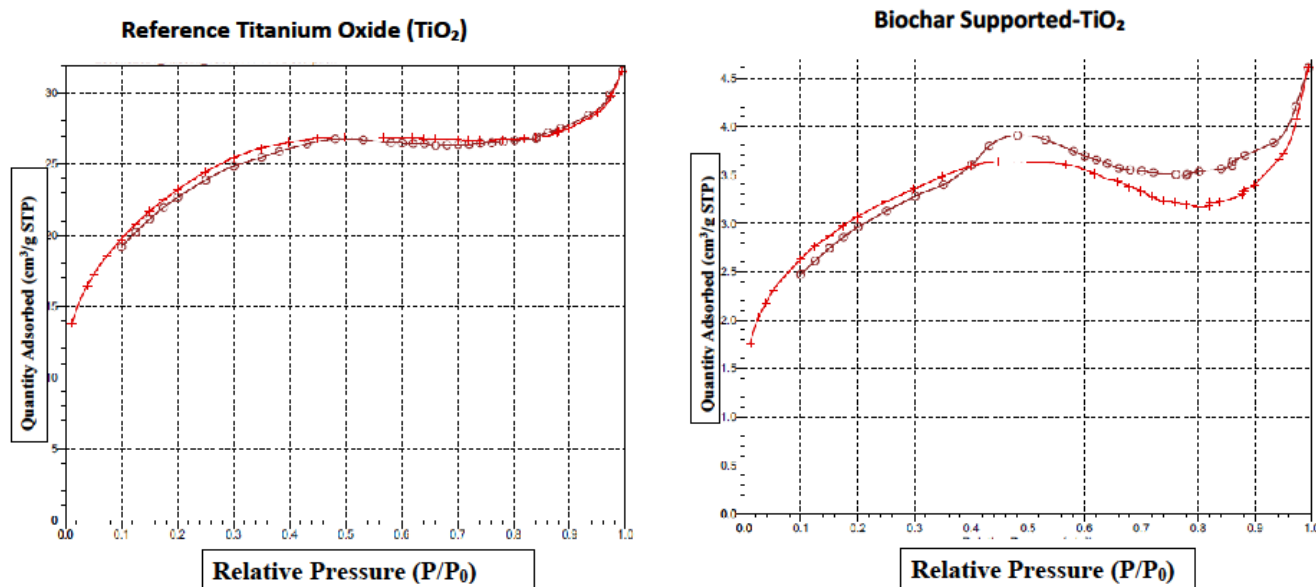


Figure 3. Brunauer–Emmett–Teller (BET) nitrogen adsorption–desorption isotherms of the reference titanium oxide nanoparticles and biochar-supported titanium oxide nanoparticles.

The increased BET surface area and average pore diameter of the biochar-supported titanium oxide nanoparticles indicate a reduction in the surface of titanium oxide as a result of the presence of biochar. The higher surface area and adsorption pore diameter in biochar-supported titanium oxide nanoparticles ensure higher contact time, enhanced adsorption, and photocatalytic efficiency [34].

5.7. X-ray Diffraction (XRD) Analysis

The X-ray diffraction (XRD) patterns of titanium oxide and biochar-supported titanium oxide nanoparticles are provided in Figure 4. In these patterns, all lines can be indexed using the ICDD No. 00-001-1292. The position of 2θ corresponds to Miller indices of the (110), (101), (111), (211), (220), (002), and (301) crystalline planes. The distinctive peaks at 2θ angles in the synthesized TiO_2 corresponded to the rutile phase. These peaks are similar for both the reference titanium oxide and the biochar-supported titanium oxide nanoparticles. Meanwhile, the distinct peaks in biochar-supported titanium oxide nanoparticles at the (220), (301), and (200) crystalline planes showed the characteristic anatase phase. Therefore, there was a mixture of rutile and anatase crystalline phases in the biochar-supported titanium oxide nanoparticles due to the influence of biochar. According to Zhang (2017) [34], photocatalysts with anatase and rutile phases are more efficient than those with only one crystalline phase.

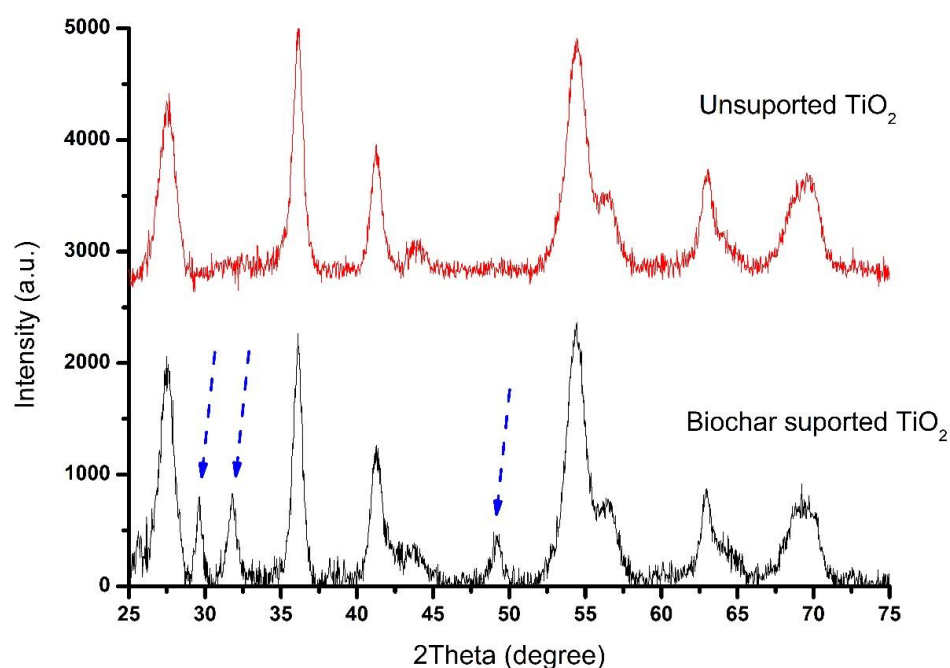


Figure 4. XRD pattern of titanium oxide and biochar-supported titanium oxide nanoparticles.

5.8. Application of the Biochar-Supported Titanium Oxide Nanoparticles for the Degradation of Orange II Sodium Azo-Dye

The abilities of the biochar-supported titanium oxide nanoparticles to act as a photocatalyst at various reaction conditions were investigated through the photochemical degradation (visible light) of an Orange II Sodium (OR2) salt in simulated textile wastewater. A quantity of OR2 equal to 100 mL in a 250 mL glass container was subjected to degradation (100 rpm, 30 degrees Celsius) by exposure to a 160 W Mega-Ray irradiation lamp light with a UV filter (less than 450 nm). The solution was initially set up and left in the dark for 20 min to allow the adsorption–desorption equilibrium between the photocatalyst (titanium oxide) and OR2 molecules. The reaction setup was subjected to various conditions, as presented in Table 4. Thereafter, the samples were centrifuged and then analyzed with the aid of a UV–visible spectrophotometer to determine the % degradation.

The calibration curve for the absorption spectra of Orange II Sodium salt (OR2) for concentrations ranging from 2 ppm to 10 ppm was obtained by measuring the respective absorbance of the prepared OR2 concentration ($\lambda_{\text{max}} = 483 \text{ nm}$). This was done in order to be able to determine the concentrations of OR2 during the batch photodegradation experiments.

Table 4. Reaction design for the application of photocatalysts.

OR2 Concentration (ppm)	Amount of Photocatalyst (mg/L)	Time (min)	OR2 Solution pH
20	50	60	6.8
30	50	60	6.8
40	50	60	6.8
50	50	60	6.8
20	50	60	6.8
20	100	60	6.8
20	150	60	6.8
20	200	60	6.8
20	50	5	6.8
20	50	10	6.8
20	50	15	6.8
20	50	20	6.8
20	50	60	4.0
20	50	60	6.0
20	50	60	8.0
20	50	60	10.0

5.9. Effect of Photocatalyst Loading

Amounts of the synthesized titanium oxide and biochar-supported titanium oxide nanoparticles between 50 mg/L and 200 mg/L were applied in a reaction chamber for the photodegradation reaction of OR2 under solar irradiation. The OR2 photodegradation was very poor (12.47%) when the synthesized titanium oxide was applied, and there was no significant improvement in the OR2 photodegradation despite an increase in the photocatalyst dosage. Meanwhile, biochar-supported titanium oxide nanoparticles gave a relatively higher % photodegradation (28.58%) with an increase in degradation efficiency (55.34) with an increase in the amount of the biochar-supported titanium oxide nanoparticles (Figure 5).

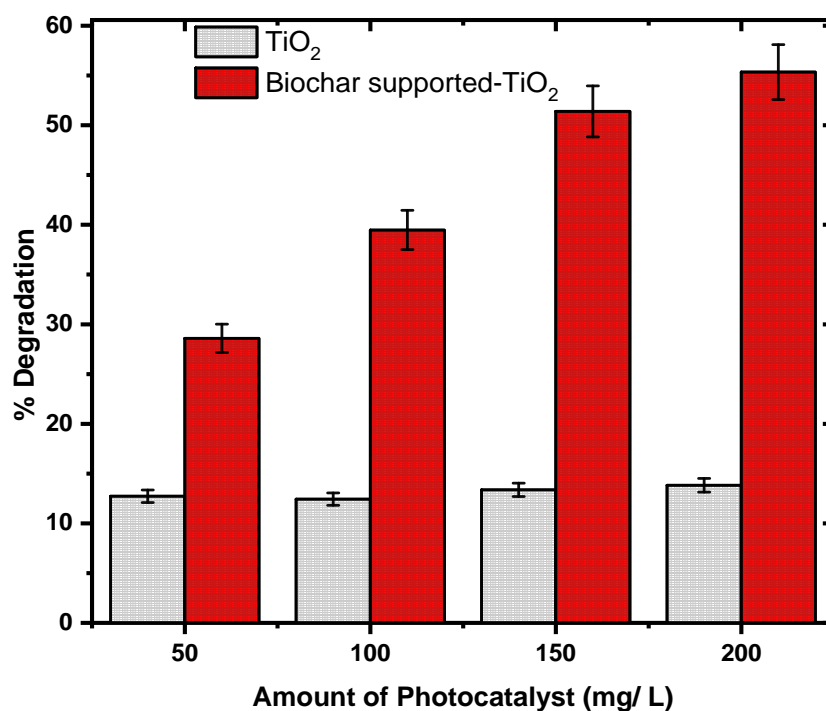


Figure 5. Effect of photocatalyst loading on the efficiency of photodegradation of OR2 (OR2 concentration = 20 ppm, pH = 6.8, exposure time = 60 min).

The photodegradation efficiency of OR2 during the application of biochar-supported titanium oxide nanoparticles was directly proportional to the catalyst loading. This indicated a true catalytic regime that can be attributed to the increased photoreactive sites on the surface of biochar. Meanwhile, the observed 12.47% degradation during solar irradiation in the presence of the synthesized reference titanium oxide nanoparticles may be accounted for by its adsorption of OR2. The photoreactivity of titanium was very poor under solar irradiation, and it was evident that the enhancement of % degradation in the biochar-supported titanium oxide nanoparticles was caused by the presence of biochar in the titanium oxide system [35]. The noticed reduction in photodegradation efficiencies in biochar-supported titanium oxide nanoparticles was due to the increased turbidity of the OR2 solution and the consequential low light penetration [8].

5.10. Impact of Solution pH on Photodegradation of OR2

The photocatalytic efficiency of the biochar-supported titanium oxide nanoparticles was strongly affected by the OR2 solution pH. The highest photocatalytic efficiency of OR2 was recorded for the biochar-supported titanium oxide nanoparticles (83.48%) at pH 6, while the lowest (73.08%) was attained at pH 10 (Figure 6). The results showed the significant influence of solution pH and that acidic and neutral pH conditions were more favorable than basic conditions. This suggests that the photophysical generation of free radical oxidants such as hydroxyl radicals was more intense in acidic and neutral OR2 solutions [36].

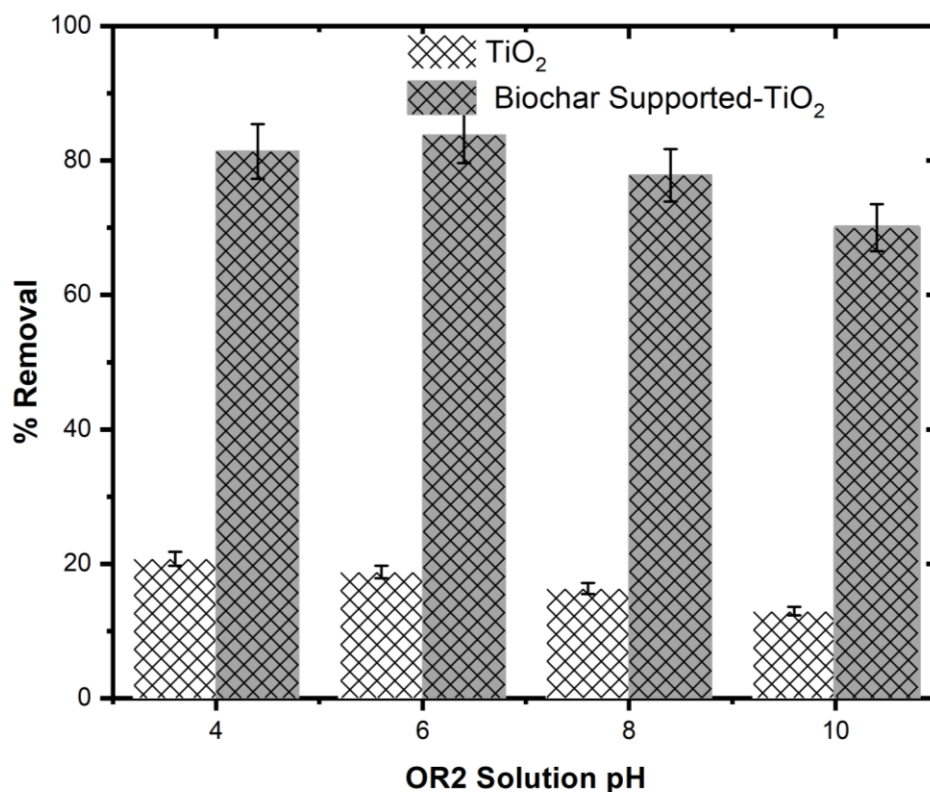


Figure 6. The percentage photodegradation of OR2 solution at varied pH.

A higher photocatalytic efficiency was observed in a neutral medium due to the non-dissociative nature of the dye which led to a strong adsorption onto the catalyst surface. The noticed decrease in photodegradation efficiency was a resultant effect of the negatively charged nature of the photocatalyst surface and the resultant poor surface activity in a basic medium [37]. A photocatalyst with optimum efficiency at neutral pH is highly desirable because there will not be a need for costly post-treatment pH adjustment.

5.11. Effect of Initial Dye Concentration

A decreased photodegradation efficiency was noticed as the concentration of OR2 exceeded 20 ppm (Figure 7). This can be accounted for by the opaque nature of the concentrated OR2 which prevented the photodegradation by blocking the white light penetration during irradiation. The photocatalyst mainly acted as a catalyst; therefore, its concentration must be kept at a certain low quantity. This implies that well-diluted textile wastewater is required for photocatalytic treatment. In addition, photodegradation may be more efficient in the tertiary stages of water treatment [38].

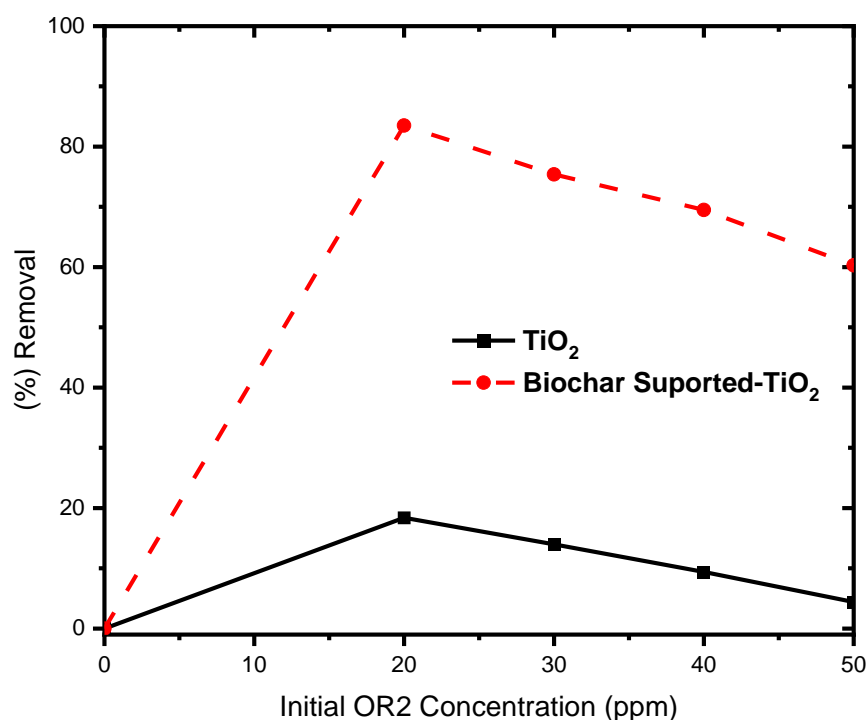


Figure 7. Effect of initial dye concentration on the photodegradation efficiency of OR2 [Ccat = 200 mg/L, pH = 6.8, time = 60 min].

5.12. Kinetics of the Photodegradation of Orange II Sodium Dye

The kinetic studies for OR2 photodegradation using both synthesized titanium oxide and biochar-supported titanium oxide nanoparticles are presented (Figure 8). The photodegradation of OR2 by the photocatalysts followed the pseudo-first-order model and aligned with the Langmuir–Hinshelwood kinetic model with the assumption that the catalyst's surface sites are energetically homogeneous [24]. This led to the observed linear reciprocal relation between the reaction rate and the concentration of reaction substrate in a solution (Equation (2)).

$$r = \frac{ksKC}{(KC + 1')} \quad (2)$$

Here, r , k , K , s , and C represent the rate of the reaction, rate constant of the reaction of the surface-adsorbed substrate with e^- (h^+), adsorption equilibrium constant, limiting amount of surface adsorption, and concentration of substrate in the bulk equilibrium, respectively.

The high values of the coefficient of determination (r^2) obtained in the kinetic plots of the current investigations imply good correlation values in the linear regression models. This showed that the photodegradation processes of OR2 in the presence of the synthesized titanium oxide nanoparticles and biochar-supported titanium oxide nanoparticles were governed by the pseudo-first-order kinetic model [37,39]. The K values for the synthesized titanium oxide nanoparticles and biochar-supported titanium oxide nanoparticles were compared (Table 5). It became apparent that the prepared synthesized titanium oxide

nanoparticles had a lower photocatalytic activity under visible light in comparison with the biochar-supported titanium oxide nanoparticles.

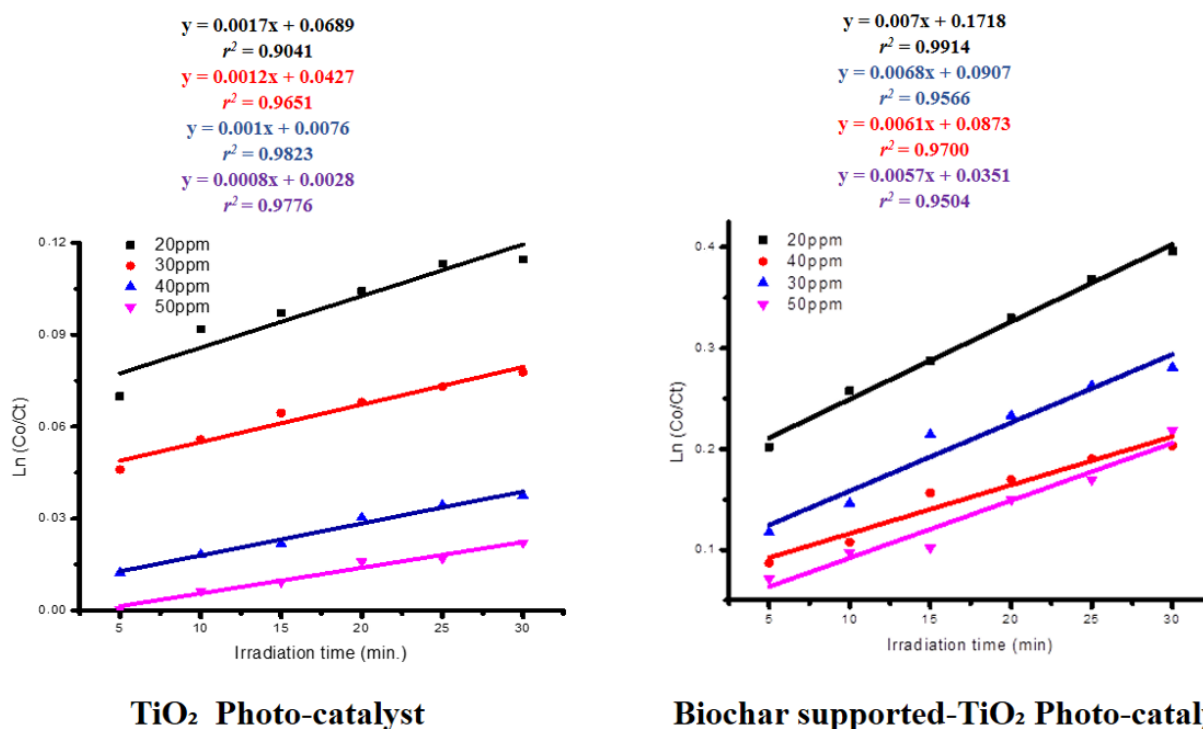


Figure 8. The photodegradation kinetics of OR2 in the synthesized titanium oxide and biochar-supported titanium oxide nanoparticles [Ccat = 200 mg/L, pH = 6.8].

Table 5. Kinetic parameters of OR2 photodegradation in the synthesized titanium oxide nanoparticles and the biochar-supported titanium oxide nanoparticles.

Photocatalyst	OR2 Concentration (ppm)	$K_1 \times 10^{-3}$ (s ⁻¹)	r^2	1/K (s)
Synthesized Titanium Oxide Nanoparticles	20	10.2	0.9041	98.3
	30	7.5	0.9651	132.7
	40	4.9	0.9823	202.2
	50	2.2	0.9776	442.8
Biochar-Supported Titanium Oxide Nanoparticles	20	15	0.9914	66.7
	30	13.2	0.9566	75.8
	40	9.8	0.9700	102
	50	7.8	0.9504	128.2

5.13. Electrical Energy Efficiency Per Order (EE_O) of the Photocatalytic Degradation of OR2

The electrical energy per order (EE_O) is the kilowatt hours of electrical energy required to degrade a (90%) contaminant's concentration per one order of magnitude per cubic meter of solution. It is a measure of photocatalyst efficiency in the degradation of persistent organic/inorganic pollutants. Lower EE_O values are required for an efficient photocatalyst, and the photocatalytic degradation of organic and inorganic pollutants is classified as a high-energy process with median EE_O values of 335 kWh/m³ [40]. The EE_O of the prepared titanium oxide nanoparticles and that of the biochar-supported titanium oxide nanoparticles are presented in Table 6. It was observed that the EE_O values of the synthesized titanium oxide nanoparticles were very high (between 1056.75 and 1770.58 kWh/m³) across the tested contaminant pH range. Meanwhile, the EE_O values of the biochar-supported titanium oxide nanoparticles were very low (between 136.49 and 187.22 kWh/m³) across

the same pH range. The results confirm that photocatalytic degradation is affected by the solution pH and that the photocatalyst has the best efficiency at the contaminant solution pH 6.8 for the biochar-supported titanium oxide nanoparticles. In addition, it can be observed that the biochar-supported titanium oxide nanoparticles offered a better energy efficiency at all tested pH values compared to the synthesized titanium oxide nanoparticles.

Table 6. Electrical energy efficiency per order (EE_o) and kinetic parameters of OR2 for the synthesized titanium oxide nanoparticles and biochar-supported titanium oxide nanoparticles at varied solution pH [OR2 concentration = 20 ppm, Photocatalyst concentration = 200 mg/L, Time = 60 min, power = 160 W].

Photocatalyst	pH	Removal (%)	$K \times 10^{-3}$ (min ⁻¹)	r^2	EE _o (kWh/m ³)
Synthesized Titanium Oxide Nanoparticles	4	20.75	1.94	0.7170	1056.75
	6.8	18.77	1.73	0.7719	1182.19
	8	16.32	1.49	0.8766	1379.36
	10	12.96	1.16	0.8273	1770.58
Biochar-Supported Titanium Oxide Nanoparticles	4	81.73	14.17	0.9549	144.57
	6.8	83.48	15.01	0.9525	136.49
	8	77.81	12.53	0.9677	163,39
	10	70.03	10.94	0.9435	187.22

6. Conclusions

The limitations in the photocatalytic application of titanium oxide nanoparticles such as a high energy bandgap and electron recombination were overcome by modification through the synthesis of biochar-supported titanium oxide nanoparticles. A massive reduction in the energy bandgap of 1.96 eV was achieved in the mixed anatase/rutile biochar-supported titanium oxide nanoparticles. Characterization of the synthesized biochar-supported titanium oxide nanoparticles which was performed using SEM-EDS revealed the appearance of an oxygen vacancy on the titanium nanoparticle surface. Meanwhile, the XRD and BET analyses respectively showed that the titanium was successfully immobilized on the biochar external surface and that the biochar-supported titanium nanoparticles had an enhanced surface area. In addition, the synthesized biochar-supported titanium oxide nanoparticles exhibited a small hysteresis phenomenon which represents a typical type IV adsorption isotherm attributed to a mesoporous material with low porosity. The highlighted results were justified by the improved photocatalytic efficiency shown by the biochar-supported titanium oxide nanoparticles during their application as a photocatalyst in the solar irradiation of Orange II Sodium salt.

Author Contributions: Conceptualization, K.O.B.; methodology, L.K.; validation, F.W.; writing—original Draft, L.K.; writing—review and editing, K.O.B. and F.W.; supervision: F.W. All authors have read and agreed to the published version of the manuscript.

Funding: Support by Cape Peninsular University of Technology-University Research Fund (CPUT-URF).

Data Availability Statement: The data for this paper are available at the Chemistry Department, Cape Peninsular University of Technology.

Conflicts of Interest: There is no conflict of interest in the current manuscript.

References

- Zeribi, F.; Attaf, A.; Derbali, A.; Saidi, H.; Benmebrouk, L.; Aida, M.S.; Dahnoun, M.; Nouadji, R.; Ezzaouia, H. Dependence of the Physical Properties of Titanium Dioxide (TiO₂) Thin Films Grown by Sol-Gel (Spin-Coating) Process on Thickness. *ECS J. Solid State Sci. Technol.* **2022**, *11*, 023003. [[CrossRef](#)]
- Pelaez, M.; Nolan, N.T.; Pillai, S.C.; Seery, M.K.; Falaras, P.; Kontos, A.G.; Dunlop, P.S.M.; Hamilton, J.W.J.; Byrne, J.A.; O'Shea, K.; et al. A review on the visible light active titanium dioxide photocatalysts for environmental applications. *Appl. Catal. B Environ.* **2012**, *125*, 331–349. [[CrossRef](#)]

3. Hofierka, J.; Kaňuk, J. Assessment of photovoltaic potential in urban areas using open-source solar radiation tools. *Renew. Energy* **2009**, *34*, 2206–2214. [[CrossRef](#)]
4. Rashed, M.N.; Eltahir, M.A.; Abdou, A.N.A. Adsorption and photocatalysis for methyl orange and Cd removal from wastewater using TiO₂/sewage sludge-based activated carbon nanocomposites. *R. Soc. Open Sci.* **2017**, *4*, 170834. [[CrossRef](#)] [[PubMed](#)]
5. Guo, Q.; Zhou, C.; Ma, Z.; Yang, X. Fundamentals of TiO₂ Photocatalysis: Concepts, Mechanisms, and Challenges. *Adv. Mater.* **2019**, *31*, 1–26. [[CrossRef](#)] [[PubMed](#)]
6. Chang, J.; Zhang, Q.; Liu, Y.; Shi, Y.; Qin, Z. Preparation of Fe₃O₄/TiO₂ magnetic photocatalyst for photocatalytic degradation of phenol. *J. Mater. Sci. Mater. Electron.* **2018**, *29*, 8258–8266. [[CrossRef](#)]
7. Hengerer, R.; Bolliger, B.; Erbudak, M.; Grätzel, M. Structure and stability of the anatase TiO₂ (101) and (001) surfaces. *Surf. Sci.* **2000**, *460*, 162–169. [[CrossRef](#)]
8. Luo, X.; Zhu, S.; Wang, J.; Wang, C.; Wu, M. Characterization and computation of Yb/TiO₂ and its photocatalytic degradation with benzohydroxamic acid. *Int. J. Environ. Res. Public Health* **2017**, *14*, 1471. [[CrossRef](#)]
9. de Oliveira Pereira, L.; Marques Sales, I.; Pereira Zampiere, L.; Silveira Vieira, S.; do Rosário Guimarães, I.; Magalhães, F. Preparation of magnetic photocatalysts from TiO₂, activated carbon and iron nitrate for environmental remediation. *J. Photochem. Photobiol. A Chem.* **2019**, *382*, 111907. [[CrossRef](#)]
10. Avilés-García, O.; Espino-Valencia, J.; Romero-Romero, R.; Rico-Cerda, J.L.; Arroyo-Albiter, M.; Solís-Casados, D.A.; Natividad-Rangel, R. Enhanced Photocatalytic Activity of Titania by Co-Doping with Mo and W. *Catalysts* **2018**, *8*, 631. [[CrossRef](#)]
11. Wong, T. ScienceDirect Smog induces oxidative stress and microbiota disruption. *J. Food Drug Anal.* **2017**, *477*, 1–10. [[CrossRef](#)]
12. Jiang, W.; Pelaez, M.; Dionysiou, D.D.; Entezari, M.H.; Tsoutsou, D.; O’Shea, K. Chromium(VI) removal by maghemite nanoparticles. *Chem. Eng. J.* **2013**, *222*, 527–533. [[CrossRef](#)]
13. Mahlambi, M.M.; Ngila, C.J.; Mamba, B.B. Recent Developments in Environmental Photocatalytic Degradation of Organic Pollutants: The Case of Titanium Dioxide Nanoparticles-A Review. *J. Nanomater.* **2015**, *2015*, 790173. [[CrossRef](#)]
14. Badmus, K.O.; Wewers, F.; Al-Abri, M.; Shahbaaz, M.; Petrik, L.F. Synthesis of oxygen deficient TiO₂ for improved photocatalytic efficiency in solar radiation. *Catalysts* **2021**, *11*, 904. [[CrossRef](#)]
15. Bourquard, F.; Bleu, Y.; Loir, A.-S.; Caja-Munoz, B.; Avila, J.; Asensio, M.-C.; Raimondi, G.; Shokouhi, M.; Rassas, I.; Farre, C.; et al. Electroanalytical Performance of Nitrogen-Doped Graphene Films Processed in One Step by Pulsed Laser Deposition Directly Coupled with Thermal Annealing. *Materials* **2019**, *12*, 666. [[CrossRef](#)] [[PubMed](#)]
16. Mohammadi, F.M.; Ghasemi, N. Influence of temperature and concentration on biosynthesis and characterization of zinc oxide nanoparticles using cherry extract. *J. Nanostructure Chem.* **2018**, *8*, 93–102. [[CrossRef](#)]
17. Hejri, Z.; Hejri, M.; Omidvar, M.; Morshedi, S. Synthesis of TiO₂/nZVI nanocomposite for nitrate removal from aqueous solution. *Int. J. Ind. Chem.* **2019**, *10*, 225–236. [[CrossRef](#)]
18. Kang, X.; Liu, S.; Dai, Z.; He, Y.; Song, X.; Tan, Z. Titanium dioxide: From engineering to applications. *Catalysts* **2019**, *9*, 191. [[CrossRef](#)]
19. Yanhui, A.; Wang, K.; Wang, P.; Wang, C.; Hou, J. Synthesis of novel 2D-2D p-n heterojunction BiOBr/La₂Ti₂O₇ composite photocatalyst with enhanced photocatalytic performance under both UV and visible light irradiation. *Appl. Catal. B Environ.* **2016**, *194*, 157–168. [[CrossRef](#)]
20. Abel, S.; Jule, L.T.; Belay, F.; Shanmugam, R.; Dwarampudi, L.P.; Nagaprasad, N.; Krishnaraj, R. Application of Titanium Dioxide Nanoparticles Synthesized by Sol-Gel Methods in Wastewater Treatment. *J. Nanomater.* **2021**, *2021*, 3039761. [[CrossRef](#)]
21. Castro, A.M.; Lopes, I.; Rocha-santos, T. Evaluation of the Potential Toxicity of Effluents from the Textile Industry before and after Treatment. *Appl. Sci.* **2019**, *9*, 3804. [[CrossRef](#)]
22. Chiu, Y.H.; Chang, T.F.M.; Chen, C.Y.; Sone, M.; Hsu, Y.J. Mechanistic insights into photodegradation of organic dyes using heterostructure photocatalysts. *Catalysts* **2019**, *9*, 430. [[CrossRef](#)]
23. Subramani, A.K.; Byrappa, K.; Ananda, S.; Lokanatha Rai, K.M.; Ranganathaiah, C.; Yoshimura, M. Photocatalytic degradation of indigo carmine dye using TiO₂ impregnated activated carbon. *Bull. Mater. Sci.* **2007**, *30*, 37–41. [[CrossRef](#)]
24. Singh, P.; Vishnu, M.C.; Sharma, K.K.; Singh, R.; Madhav, S.; Tiwary, D.; Mishra, P.K. Comparative study of dye degradation using TiO₂-activated carbon nanocomposites as catalysts in photocatalytic, sonocatalytic, and photosonocatalytic reactor. *Desalin. Water Treat.* **2016**, *57*, 20552–20564. [[CrossRef](#)]
25. Nguyen, C.H.; Tran, H.N.; Fu, C.C.; Lu, Y.T.; Juang, R.S. Roles of adsorption and photocatalysis in removing organic pollutants from water by activated carbon-supported titania composites: Kinetic aspects. *J. Taiwan Inst. Chem. Eng.* **2020**, *109*, 51–61. [[CrossRef](#)]
26. Mondol, B.; Sarker, A.; Shareque, A.M.; Dey, S.C.; Islam, M.T.; Das, A.K.; Shamsuddin, S.M.; Molla, M.A.I.; Sarker, M. Preparation of Activated Carbon/TiO₂ Nanohybrids for Photodegradation of Reactive Red-35 Dye Using Sunlight. *Photochem* **2021**, *1*, 54–66. [[CrossRef](#)]
27. Lian, W.; Yang, L.; Joseph, S.; Shi, W.; Bian, R.; Zheng, J.; Li, L.; Shan, S.; Pan, G. Utilization of biochar produced from invasive plant species to efficiently adsorb Cd (II) and Pb (II). *Bioresour. Technol.* **2020**, *317*, 124011. [[CrossRef](#)]
28. Xu, J.; Cui, K.; Gong, T.; Zhang, J.; Zhai, Z.; Hou, L.; Zaman, F.U.; Yuan, C. Ultrasonic-Assisted Synthesis of N-Doped, Multicolor Carbon Dots toward Fluorescent Inks, Fluorescence Sensors, and Logic Gate Operations. *Nanomaterials* **2022**, *12*, 312. [[CrossRef](#)]

29. Nguyen, L.T.; Nguyen, H.T.; Pham, T.D.; Tran, T.D.; Chu, H.T.; Dang, H.T.; Nguyen, V.H.; Nguyen, K.M.; Pham, T.T.; Van der Bruggen, B. UV-Visible Light Driven Photocatalytic Degradation of Ciprofloxacin by N,S Co-doped TiO₂: The Effect of Operational Parameters. *Top. Catal.* **2020**, *63*, 985–995. [[CrossRef](#)]
30. Pudza, M.Y.; Abidin, Z.Z.; Rashid, S.A.; Yasin, F.M.; Noor, A.S.M.; Issa, M.A. Eco-friendly sustainable fluorescent carbon dots for the adsorption of heavy metal ions in aqueous environment. *Nanomaterials* **2020**, *10*, 315. [[CrossRef](#)]
31. Singh, R.K.; Kumar, R.; Singh, D.P. Graphene oxide: Strategies for synthesis, reduction and frontier applications. *RSC Adv.* **2016**, *6*, 64993–65011. [[CrossRef](#)]
32. Eppa, R.; Durgam, K.; Ramana, M.V.; Reddy, S.R.; Sivakumar, J. Structural, Optical and Photocatalytic Properties of Anatase/Rutile TiO₂ Nanoparticles. *i-Manag. J. Mater. Sci.* **2018**, *6*, 43. [[CrossRef](#)]
33. Wang, X.; Cai, W.; Lin, Y.; Wang, G.; Liang, C. Mass production of micro/nanostructured porous ZnO plates and their strong structurally enhanced and selective adsorption performance for environmental remediation. *J. Mater. Chem.* **2010**, *20*, 8582–8590. [[CrossRef](#)]
34. Zhang, F. Grand Challenges for Nanoscience and Nanotechnology in Energy and Health. *Front. Chem.* **2017**, *5*, 80. [[CrossRef](#)]
35. Tong, Y.; Shi, G.; Hu, G.; Hu, X.; Han, L.; Xie, X.; Xu, Y.; Zhang, R.; Sun, J.; Zhong, J. Photo-catalyzed TiO₂ inactivates pathogenic viruses by attacking viral genome. *Chem. Eng. J.* **2021**, *414*, 128788. [[CrossRef](#)] [[PubMed](#)]
36. Kumari, M.; Pittman, C.U.; Mohan, D. Heavy metals [chromium (VI) and lead (II)] removal from water using mesoporous magnetite (Fe₃O₄) nanospheres. *J. Colloid Interface Sci.* **2015**, *442*, 120–132. [[CrossRef](#)] [[PubMed](#)]
37. Ali, Z.; Mehmood, M.; Ahmed, J.; Nizam, M.N. Synthesis of graphitic nanofibers and carbon nanotubes by catalytic chemical vapor deposition method on nickel chloride alcogel for high oxygen evolution reaction activity in alkaline media. *Nano-Struct. Nano-Objects* **2020**, *24*, 100574. [[CrossRef](#)]
38. Bhati, M.; Rai, R. Nanotechnology and water purification: Indian know-how and challenges. *Environ. Sci. Pollut. Res.* **2017**, *24*, 23423–23435. [[CrossRef](#)]
39. Madhvi; Singh, L.; Saroj, S.; Lee, Y.; Singh, S.V. Facile synthesis of nano-crystalline anatase TiO₂ and their applications in degradation of Direct blue 199. *J. Mater. Sci. Mater. Electron.* **2016**, *27*, 2581–2588. [[CrossRef](#)]
40. Guaraldo, T.T.; Vakili, R.; Wenk, J.; Mattia, D. Highly efficient ZnO photocatalytic foam reactors for micropollutant degradation. *Chem. Eng. J.* **2023**, *455*, 140784. [[CrossRef](#)]

Disclaimer/Publisher's Note: The statements, opinions and data contained in all publications are solely those of the individual author(s) and contributor(s) and not of MDPI and/or the editor(s). MDPI and/or the editor(s) disclaim responsibility for any injury to people or property resulting from any ideas, methods, instructions or products referred to in the content.